FRACTIONAL ABUNDANCE ESTIMATION OF MIXED AND COMPOUND MATERIALS BY HYPERSPECTRAL IMAGING.

Bikram Koirala[1]*, Zohreh Zahiri*[1]*, Mahdi Khodadadzadeh*[2]*, Paul Scheunders*[1]

[1] Imec-Visionlab, University of Antwerp, Belgium
[2] Helmholtz Institute Freiberg for Resource Technology, Germany

ABSTRACT

The mechanical and chemical properties of a compound material are determined by the fractional abundances of its components. In this work, we present a spectral unmixing technique to estimate the fractional abundances of the components of mixed and compound materials from hyperspectral images. The estimation of fractional abundances in mixed materials faces the main challenge of intimate mixing. In compound materials, the mixing with water causes changes in chemical properties resulting in spectral variability and non-linearity. To address these challenges, a supervised method is proposed that learns a mapping from the hyperspectral data to spectra that follow the linear mixing model. Then, a linear unmixing technique is applied on the mapped spectra to estimate the fractional abundances. To demonstrate the potential of the proposed method, experiments are conducted on hyperspectral images from mixtures of red and yellow clay powders and hardened mortar samples with varying water to cement ratios.

1. INTRODUCTION

In remote sensing, hyperspectral imaging has been applied for many years for urban, geological, and agricultural studies. With advances in hyperspectral sensor technology, low cost hyperspectral cameras became available that can be applied in close-range settings for fast, economical, and non-destructive material characterization. Specifically, hyperspectral imaging is an effective tool to estimate the mechanical and chemical properties of construction materials. In [1], spectrometry data was used to determine bricks characteristics. In [2], concrete and cement-based materials with different water to cement ratio (w/c) were characterized by hyperspectral imaging. The spectral analysis in these studies was done by supervised classification of the different compositions, without using any reference spectral data related to the ingredients (cement, sand, gravel, water, red clay, yellow clay).

Model-based spectral unmixing techniques estimate the fractional abundances of the different materials within a hyperspectral pixel by minimizing the error between the true reflectance spectrum and the spectrum that is generated by a particular mixing model. When the incoming rays of light interact with a single pure material in the pixel before reaching the sensor, the linear mixing model (LMM) [3] can estimate the material fractions accurately. In intimate mixture scenarios, the incoming rays of light interact with more than one pure material making the true reflectance spectrum a highly nonlinear mixture of the pure materials (i.e., endmembers). To solve this problem, several nonlinear mixing models have been developed [4].

One of the drawbacks of the model-based approaches is that not all spectra necessarily follow the same nonlinear mixing model. Moreover, the model parameters can be hard to interpret and link to the actual fractional abundances. However, the main problem with compound materials is that the pure materials change their reflectance properties when reacting with water. This result in endmember variability and a loss of the relation between the endmember spectra and the fractional abundances.

Recently, we proposed a neural network based method [5] that uses training data to learn a mapping from nonlinear spectra to spectra that follow the linear mixing model, after which the LMM is applied for the estimation of the actual fractional abundances. In this paper, we adopt a similar strategy and test three different nonlinear methods to learn the mapping. This mapping procedure tackles both the nonlinearities in intimate mixtures and the changes in the chemical properties of the pure materials. Once the mapping is learned, all spectra from test samples are mapped to the linear model and the mapped spectra are unmixed by applying the LMM to estimate the fractional abundances. The presented methodology is validated on mixtures from red and yellow clay powders with different fractional compositions and three mortar samples with varying water to cement ratio.

2. METHODOLOGY

Let us consider a matrix containing N reflectance spectra $\mathbf{X}(\{\mathbf{x}_i\}_{i=1}^{N} \in \mathbf{R}_{+}^{d})$ and a set of p pure spectra (endmembers) $\mathbf{E}(\{\mathbf{e}_j\}_{j=1}^{p} \in \mathbf{R}_{+}^{d})$. The LMM construct a spectrum $\mathbf{x}_i$ by combining endmembers linearly:

$$\mathbf{x}_i = \sum_{j=1}^{p} a_j \mathbf{e}_j + \boldsymbol{\eta} = \mathbf{E}\mathbf{a} + \boldsymbol{\eta} \tag{1}$$

where a_j is the fractional abundance of endmember $\mathbf{e}_j$ and $\boldsymbol{\eta}$ represents Gaussian noise. The fractional abundance of each spectrum is estimated by minimizing $\|\mathbf{x}_i - \mathbf{E}\mathbf{a}\|^2$ under the physical constraints: $\sum_j a_j = 1, \forall j : a_j \geq 0$.

We propose to learn a mapping from the nonlinear spectra to the LMM ([5]). A training set with known endmember spectra and fractional abundances $(\mathbf{E}, \{\mathbf{a}_i\}_{i=1}^n)$ is applied to generate linear spectra $\mathbf{X}_l = \{\mathbf{x}_i\}_{i=1}^n$ and for learning a mapping between the actual spectra $\mathbf{Y} = \{\mathbf{y}_i\}_{i=1}^n$ and the linear ones. This mapping can be learned by applying different machine learning regression algorithms. In this work, we choose feedforward neural networks (NN), as in [5], kernel ridge regression (KRR), and gaussian processes (GP). The mapping is then applied to map the test nonlinear spectra $\mathbf{Y}_* = \{\mathbf{y}_i\}_{i=n+1}^N$ onto linear spectra $\mathbf{X}_* = \{\mathbf{x}_i\}_{i=n+1}^N$.

2.1. Feedforward neural networks

The feedforward neural network (NN) applied in this work has three layers: the input and output layer of d nodes and a hidden layer consisting of 5 nodes. The network was trained by dividing the dataset into a training, validation, and test set. The network parameters (weights and biases) were optimized by using a training set while the validation set was used to avoid overfitting.

2.2. Kernel ridge regression

Another way to learn the mapping is given by kernel ridge regression [6][7], a kernelized extension of ridge regression. Ridge regression finds a linear relationship between the input and output by:

$$\mathbf{x}_i = \mathbf{X}_l \left(\mathbf{Y}^T \mathbf{Y} + \lambda \mathbf{I} \right)^{-1} \mathbf{Y}^T \mathbf{y}_i \tag{2}$$

where λ is a regularization parameter that tackles the problem of overfitting and $\mathbf{I}$ is the identity matrix.

Using the kernel trick, the mapping of a nonlinear spectrum $\mathbf{y}_i$ to the linear one $\mathbf{x}_i$ is obtained by:

$$\mathbf{x}_i = f(\mathbf{y}_i) = \mathbf{X}_l \left(K(\mathbf{Y}, \mathbf{Y}) + \lambda \mathbf{I} \right)^{-1} K(\mathbf{Y}, \mathbf{y}_i) \tag{3}$$

where $K(\mathbf{Y}, \mathbf{Y})$ is the matrix of kernel functions between the n training points and $K(\mathbf{Y}, \mathbf{y}_i)$ is the vector of kernel functions between the n training points and a test sample. For this work, the RBF kernel is used.

$$k(\mathbf{y}_i, \mathbf{y}_j) = \exp\left(-\frac{\|\mathbf{y}_i - \mathbf{y}_j\|^2}{2\sigma^2} \right) \tag{4}$$

where σ is the kernel parameter, that controls the smoothness of the prediction function.

2.3. Gaussian processes

A Bayesian method for learning the nonlinear relationship between the input $\mathbf{Y}$ and output $\mathbf{X}_l$ is given by Gaussian processes (GP) [8]. The mean prediction of the input according to GP is obtained by factorizing the joint distribution of the training output ($\mathbf{X}_l$) and the test output ($f(\mathbf{Y}_*) = \mathbf{X}_*$), i.e., $p(f(\mathbf{Y}_*^T), \mathbf{X}_l^T)$, into the predictive distribution $p(f(\mathbf{Y}_*^T)|\mathbf{X}_l^T)$ and the marginal $p(\mathbf{X}_l^T)$. The estimated mapping of the nonlinear spectra $\mathbf{Y}_*$ to the linear spectra $\mathbf{X}_*$ is then given by:

$$\begin{aligned} \mathbf{X}_* &= f(\mathbf{Y}_*) \\ &= \mathbf{X}_l (K(\mathbf{Y}, \mathbf{Y}) + \sigma_n^2 \mathbf{I})^{-1} K(\mathbf{Y}_*, \mathbf{Y})^T \end{aligned} \tag{5}$$

where σ_n^2 is the noise variance of the training spectra. The kernel function used in (5) provides the covariance of the output:

$$cov(\mathbf{x}_i, \mathbf{x}_j) = k(\mathbf{x}_i, \mathbf{x}_j) = \sigma_f^2 \exp\left(-\sum_{b=1}^{d} \frac{\left(x_i^b - x_j^b\right)^2}{2 l_b^2} \right)$$

where σ_f^2 is the variance of the input spectra, and l_b is a characteristic length-scale for each band. The hyperparameters involved in (6) were optimized by minimizing the log marginal likelihood of the training dataset $\log(p(\mathbf{X}_l^T|\mathbf{Y}^T))$.

Finally, the fractional abundances from the mapped spectra are obtained by applying the LMM.

3. EXPERIMENTAL RESULTS AND DISCUSSION

In the following experiments, the mappings are learned either by KRR, GP, or NN. For comparison, we applied a feedforward neural network to map nonlinear spectra directly to the fractional abundances, i.e., softmax (SM) and three unsupervised spectral unmixing models: the LMM, a bilinear model (the polynomial post-nonlinear model (PPNM)), and the Hapke model.

3.1. Experiment 1: clay samples

In the first experiment, two different clay powders (yellow and red) were mixed to obtain three different mixtures. The first mixture (YR5050) contains 5 g each of yellow and red clay. In the second mixture (YR6040), 6.01 g of yellow clay was mixed with 4.03 g of red clay. The third mixture (YR7030) contains 7.01 g of yellow clay and 3.03 g of red clay. The mixtures were filled in a sample holder and compressed until the top surface becomes smooth. The densities of the pure clays were estimated by weighing a 2 ml clay sample. The volume of the pure materials was computed by dividing the weight by density. The ground truth fractional abundances are the volume percentages.

Hyperspectral images were acquired from these samples as well as the pure yellow and red clay by a SPECIM

SisuRock drillcore scanner, equipped with an AisaFenix VNIR-SWIR hyperspectral sensor. Each pixel of the hyperspectral image contains 450 reflectance values for wavelengths in the range of 380-2500 nm and a spatial resolution of 1.5 mm/pixel. By using the toolbox presented in [9], radiometric, geometric and sensor-shift corrections were performed on the acquired hyperspectral images. The image of each clay mixture contains 7×7 pixels.

For the validation of the proposed techniques, only two mixtures (YR5050 and YR7030) were selected for learning the mapping. From each sample, 21 training pixels were randomly selected as training samples. By using the ground truth fractional information and the pure spectra, linearly mixed pixel spectra were generated. After learning the mapping between a hyperspectral dataset to the linear model, test spectra from not only samples YR5050 (28 pixels) and YR7030 (28 pixels) but also from sample YR6040 (49 pixels) were mapped to the linear model. Finally, the LMM was applied to estimate the fractional abundance maps.

Figure 1(a) shows the scatterplot on three spectral bands of all clay samples. Although the mixtures were homogeneous, a large spectral variation within each sample can be observed. The mapping accounts for the nonlinearities and the spectral variability caused by the intimate mixtures. The scatterplot after mapping to the linear model by NN is shown in Fig. 1(b).

Table 1 lists the estimated fractional abundances of yellow and red clay, averaged over the test pixels from YR5050, YR6040 and YR7030 (mean and standard deviations are given), and compared to the ground truth fractional abundance (GT). The obtained weights are given as well. GP outperformed the other methods on sample YR5050, SM was the best in predicting sample YR7030. Sample YR6040, although not being the part of the training, was accurately predicted by NN. The unsupervised techniques all overestimated yellow clay, while underestimating red clay. We believe that the reason for this is that the spectral reflectances of all of the mixtures are much closer to that of pure yellow clay than that of red clay.

3.2. Experiment 2: Mortar samples

In the second experiment, hardened mortar samples with three different compositions were prepared by mixing dark sand (density: 2660 Kg/m^3), cement (density: 3100 Kg/m^3), and water. The first mixture contains 1350 g of dark sand, 450 g of cement, and 270 g of water (water-to-cement (w/c) ratio (g/g) 60% (W/C60%)). The second and third mixture were prepared by only changing the amount of water to produce samples with w/c ratios of 70% (W/C70%) and 80% (W/C80%) respectively. Hyperspectral images were acquired from these samples as well as from the pure materials (dark sand and cement powders) by using the AisaFenix VNIR-SWIR hyperspectral sensor. The reflectance spectrum of water was obtained from the USGS spectral library.

Only two mortars samples (W/C60% and W/C80%) were selected for training the algorithms. From these two images, 200 training pixels (100 per sample) were randomly selected. Linearly mixed pixel spectra were generated by using the fractional abundances of the training samples and the spectra of the pure materials as endmembers. After learning the mapping, test spectra from W/C60% (1580 pixels), W/C80% (1515 pixels), and W/C70% (1785 pixels) were mapped to the linear model. Finally, the LMM was applied to estimate the abundance maps.

Figure 2(a) shows the scatterplot on three spectral bands of all mortar pixels. The plot reveals nonlinearity and spectral variability due to the intimate mixing and changes in chemical properties of the cement when mixed with water. The scatterplot after mapping to the linear model by GP is shown in Fig. 2(b). All spectra are mapped onto a linear simplex, spanned by the 3 endmembers.

Table 2 shows the estimated fractional abundances (and their standard deviations) and w/c ratio averaged over the test pixels (W/C60%, W/C70%, and W/C80%). All mapping methods estimated the abundances of dark sand, cement, and water perfectly. GP best predicted the w/c ratio for W/C60% and W/C80% while KRR best predicted W/C70%. The estimated fractional abundances from the unsupervised methods were not reliable. Cement was not detected at all, which lead to an undetermined w/c ratio. The reason can be found in the fact that the spectral reflectances of dark sand and cement are very close. Most mixed spectra are closer to dark sand than to cement, so that the reconstruction error is minimized by projecting most of the data onto the dark sand-water face of the simplex.

All methods were developed in Matlab and ran on an Intel Core $i7$-8700K CPU, 3.20 GHz machine with 6 cores. The runtimes of KRR, GP, and NN to learn the mapping from nonlinear spectra to the linear model were respectively 0.92, 241.92, and 1109.00 seconds.

4. CONCLUSIONS

In this paper, we applied a supervised method for estimating the fractions of component materials in hyperspectral data of mixed and compound materials. The method learns a mapping from the actual reflectance spectra to spectra that follow the linear mixing model. The mapping accounts for nonlinearities and spectral variability due to intimate mixtures and chemical changes. The methodology was validated on mixtures of clay powders and mortar samples. The results demonstrate the potential of the proposed technique for estimating the composition of baked bricks or the initial water to cement ratios in a hardened mortar and concrete samples. In future work, we will apply the methodology to heterogeneous mixtures, e.g., to concrete and cementitious materials.

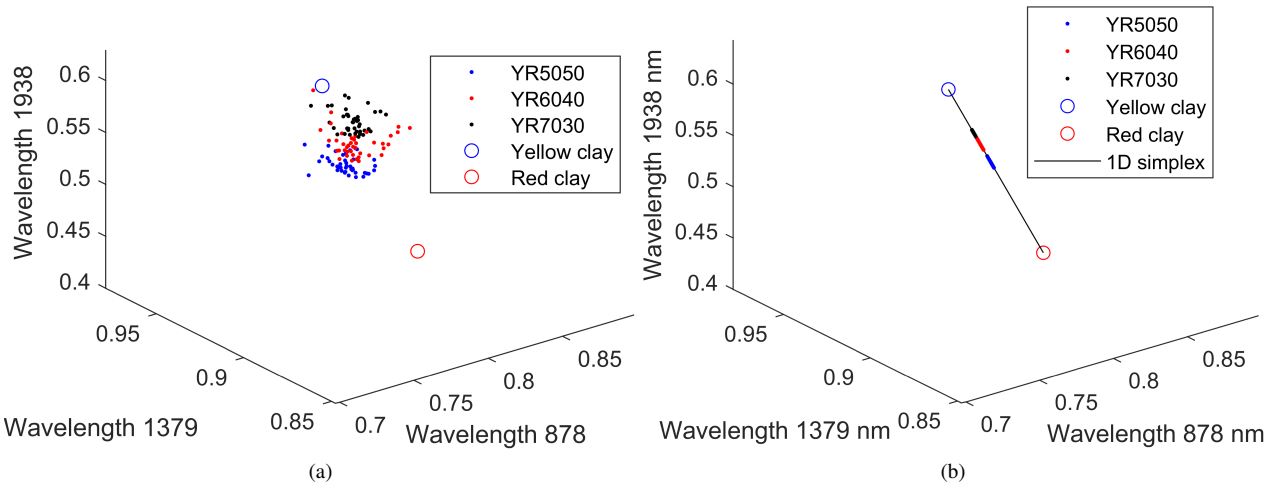

Fig. 1: Scatterplot of the clay samples; (a) true dataset; (b) after mapping to the linear model by NN. Blue, red, and black dots represent pixels from YR5050, YR6040, and YR7030 respectively.

Clay	GT	GP	KRR	NN	SM	LMM	Hapke	PPNM
				YR5050				
Yellow (%)	54	**53.97**±1.69	55.26±2.19	53.88±1.35	54.08±0.28	73.60±3.75	73.60±3.74	73.61±3.77
Red (%)	46	**46.03**±1.69	44.74±2.19	46.12±1.35	45.92±0.28	26.40±3.75	26.40±3.74	26.39±3.77
Yellow (g)	5	**5.00**	5.12	4.99	5.01	6.82	6.82	6.82
Red (g)	5	**5.00**	4.86	5.01	4.99	2.87	2.87	2.87
				YR7030				
Yellow (%)	73.09	73.16±1.20	71.22±2.05	73.22±2.53	**73.07**±0.31	92.66±3.18	92.63±3.20	92.88±3.22
Red (%)	26.91	26.84±1.20	28.78±2.05	26.78±2.53	**26.93**±0.31	7.34±3.18	7.37±3.20	7.12±3.22
Yellow (g)	7.01	7.02	6.83	7.02	**7.01**	8.89	8.88	8.91
Red (g)	3.03	3.02	3.24	3.02	**3.03**	0.83	0.83	0.80
				YR6040				
Yellow (%)	63.65	67.43±2.57	65.29±2.38	**63.79**±2.72	68.80±5.02	85.19±4.06	85.15±4.06	85.31±4.10
Red (%)	36.35	32.57±2.57	34.71±2.38	**36.21**±2.72	31.20±5.02	14.81±4.06	14.85±4.06	14.69±4.10
Yellow (g)	6.01	6.37	6.16	**6.02**	6.50	8.04	8.04	8.06
Red (g)	4.03	3.61	3.85	**4.01**	3.46	1.64	1.65	1.63

Table 1: The mean estimated fractional abundances and standard deviations (in volume %) and mean estimated weight of the test pixels by using GP, KRR, NN, SM, LMM, the Hapke model and PPNM respectively.

Endmember	GT	GP	KRR	NN	SM	LMM	Hapke	PPNM
				W/C60%				
Dark sand	55.01	**55.06**±0.63	56.70±1.52	54.84±0.45	54.59±0.38	67.57±5.24	62.90±5.51	67.42±5.20
Cement	15.74	**15.77**±0.18	14.69±0.85	15.69±0.13	15.60±0.11	0±0	0.001±0.043	0±0
Water	29.25	**29.17**±0.80	28.61±0.81	29.47±0.58	29.81±0.49	32.43±5.24	37.10±5.51	32.56±5.20
W/C ratio (%)	60	**59.70**	62.80	60.59	61.64	∞	10^6	∞
				W/C80%				
Dark sand	50.10	**50.28**±0.83	52.44±1.63	50.75±0.70	50.47±0.81	54.19±6.35	48.14±6.77	54.18±6.28
Cement	14.34	**14.39**±0.23	13.26±0.80	14.52±0.21	14.48±0.24	0±0	0±0	0±0
Water	35.56	**35.33**±1.05	34.30±1.15	34.73±0.91	35.05±1.04	45.81±6.35	51.86±6.6.77	45.82±6.28
W/C ratio (%)	80	**79.22**	83.52	77.21	78.11	∞	∞	∞
				W/C70%				
Dark sand	52.41	**53.15**±0.91	55.16±2.79	53.39±0.58	53.26±0.61	64.08±7.03	58.99±7.43	63.98±6.96
Cement	15.02	**15.15**±0.27	14.24±1.47	15.26±0.16	15.24±0.17	0±0	0±0	0±0
Water	32.57	**31.70**±1.17	30.61±1.49	31.35±0.74	31.49±0.78	35.92±7.03	41.01±7.43	36.02±6.96
W/C ratio (%)	70	67.52	**69.38**	66.26	66.66	∞	∞	∞

Table 2: The mean estimated fractional abundances, their standard deviations and mean estimated w/c ratio of test pixels (in %) by GP, KRR, NN, SM, LMM, the Hapke model, and PPNM respectively.

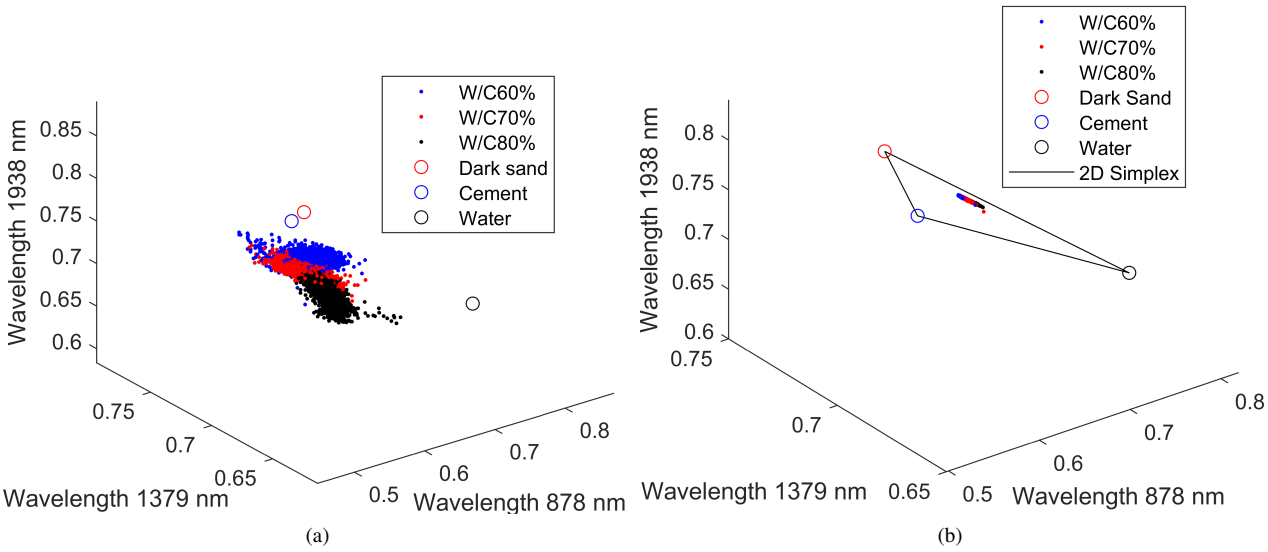

Fig. 2: Scatterplot of the mortar samples; (a) true dataset; (b) after mapping to the linear model by GP. Blue, red, and black dots represents W/C60%, W/C70%, and W/C80% respectively.

Acknowledgement

The research presented in this paper is funded by BELSPO (Belgian Science Policy Office) in the frame of the STEREO III programme – project GEOMIX (SR/06/357). The authors wish to thank Geert Jacobs and Gilles Van Loon from the Faculty of Applied Engineering (University of Antwerp), Patrick Storme from the Department of Conservation Studies (University of Antwerp), and Bert Neyens from Vandersanden Group in Belgium for their support and assistance in conducting the experimental parts of the study. Further acknowledgement should go to HZDR-HIF for providing the Drillcore Scanning facilities and conducting spectral measurements, in particular to Benjamin Melzer and Robert Zimmermann for data acquisition and Sandra Lorenz for data pre-processing.

5. REFERENCES

[1] Debra F. Laefer, Zohreh Zahiri, and Aoife Gowen, "Using short-wave infrared range spectrometry data to determine brick characteristics," *International Journal of Architectural Heritage*, vol. 0, no. 0, pp. 1–13, 2018.

[2] Zohreh Zahiri, Debra Laefer, and Aoife Gowen, "The feasibility of short-wave infrared spectrometry in assessing water-to-cement ratio and density of hardened concrete," *Construction and Building Materials*, vol. 185, pp. 661–669, 10 2018.

[3] J. W. Boardman, "Geometric mixture analysis of imaging spectrometry data," in *IEEE Intern. Geosci Remote Sens. Symp.*, 1994, pp. 2369–2371.

[4] R. Heylen, M. Parente, and P. Gader, "A review of nonlinear hyperspectral unmixing methods," *IEEE J. Sel. Topics Appl. Earth Observ. Remote Sens.*, vol. 7, no. 6, pp. 1844–1868, 2014.

[5] B. Koirala, R. Heylen, and P. Scheunders, "A neural network method for nonlinear hyperspectral unmixing," in *IEEE Intern. Geosci Remote Sens. Symp.*, 2018, pp. 4233–4236.

[6] M. Welling, *Kernel ridge regression*, Max Welling's Classnotes in Machine Learning, Toronto, 2013.

[7] J. Shawe-Taylor and N. Cristianini, *Kernel Methods for Pattern Analysis*, Cambridge University Press, Cambridge, 2004.

[8] C.K.I. Williams C.E. Rasmussen, *Gaussian Processes for Machine Learning*, The MIT Press, New York, 2006.

[9] Sandra Jakob, Robert Zimmermann, and Richard Gloaguen, "The need for accurate geometric and radiometric corrections of drone-borne hyperspectral data for mineral exploration: Mephysto—a toolbox for preprocessing drone-borne hyperspectral data," *Remote Sensing*, vol. 9, no. 1, 2017.